

Zones of Influence and Shock Motion in a Shock/Boundary-Layer Interaction

Lionel Agostini,* Lionel Larchevêque,[†] Pierre Dupont,[‡] Jean-François Debièvre,[§] and Jean-Paul Dussauge[¶]

Université de Provence, 13453 Marseille Cedex 13, France

DOI: 10.2514/1.J051516

This paper aims at describing the main features of a shock reflection on a turbulent boundary layer. The data used for this analysis are the results of large-eddy simulations of the interaction carried out with three different shock intensities: from incipient to fully separated cases. Computational results are validated vs experiments obtained for the same interaction geometries. The main space-time properties of the leading shock motions are described together with their links with the other regions of the flow. In particular, information about the origin of the shock motion is derived from the correlations between shock motion and unsteady pressure fields. It is shown that the shock motion reveals the flow unsteadiness found in the interaction region.

Nomenclature

| | |
|--------------|---|
| C | = speed of sound |
| f | = frequency |
| H_e | = elevation of crossing point between leading shock and expansion fan |
| H_i | = elevation of crossing point between incident and leading shocks |
| L | = length of interaction |
| M_c | = convective Mach number |
| St_L | = Strouhal number [see Eq. (1)] |
| St_{L_p} | = Strouhal number of disturbances along leading shock |
| U | = flow velocity |
| U_c | = convection velocity |
| U_ζ | = propagation velocity along Mach waves produced by convected sources [see Eq. (7)] |
| U_η | = propagation velocity along characteristics [see Eq. (4)] |
| U_1 | = velocity downstream of incident shock |
| V_P | = propagation velocity along shock |
| V_{P_c} | = propagation velocity along shock for disturbances associated with characteristics [Eq. (5)] |
| $V_{P_{MW}}$ | = propagation velocity along shock for disturbances associated with Mach waves [Eq. (8)] |
| X_0 | = mean position of foot of leading shock |
| X^* | = longitudinal dimensionless coordinate $(x - X_0)/L$ |
| y_1^+ | = height of cell adjacent to wall in wall unit |

Presented as Paper 2011-0728 at the 49th AIAA Aerospace Sciences Meeting including the New Horizons Forum and Aerospace Exposition, Orlando, FL, 4–7 January 2011; received 21 July 2011; revision received 24 October 2011; accepted for publication 25 October 2011. Copyright © 2012 by the American Institute of Aeronautics and Astronautics, Inc. All rights reserved. Copies of this paper may be made for personal or internal use, on condition that the copier pay the \$10.00 per-copy fee to the Copyright Clearance Center, Inc., 222 Rosewood Drive, Danvers, MA 01923; include the code 0001-1452/12 and \$10.00 in correspondence with the CCC.

*5 rue Enrico Fermi; Ph.D. Student, Institut Universitaire des Systèmes Thermiques Industriels, Unité Mixte de Recherche 7343. Student Member AIAA.

[†]5 rue Enrico Fermi; Associate Professor, Institut Universitaire des Systèmes Thermiques Industriels, Unité Mixte de Recherche 7343; lionel.larcheveque@polytech.univ-mrs.fr (Corresponding Author).

[‡]5 rue Enrico Fermi; Chargé de Recherche Centre National de la Recherche Scientifique, Institut Universitaire des Systèmes Thermiques Industriels, Unité Mixte de Recherche 7343. Senior Member AIAA.

[§]5 rue Enrico Fermi; Chargé de Recherche Centre National de la Recherche Scientifique, Institut Universitaire des Systèmes Thermiques Industriels, Unité Mixte de Recherche 7343.

[¶]5 rue Enrico Fermi; Directeur de Recherche, Centre National de la Recherche Scientifique, Institut Universitaire des Systèmes Thermiques Industriels, Unité Mixte de Recherche 7343. Senior Member AIAA.

| | |
|---------------------|--|
| Y^* | = vertical dimensionless coordinate y/L |
| α | = angle of characteristics [see Eq. (3)] |
| α' | = angle of the Mach wave [see Eq. (6)] |
| Δx^+ | = streamwise cell dimension in wall unit |
| Δz^+ | = spanwise cell dimension in wall unit |
| δ | = boundary-layer thickness |
| δ_0 | = boundary-layer thickness at inflow |
| θ | = flow deflection angle |
| λ_p | = wavelength of disturbances along leading shock |
| ξ | = distance from reference point |
| σ | = angle between shock wave and streamlines |
| τ_{opt} | = optimal delay time of cross-correlation function |

I. Introduction

SHOCK/BOUNDARY-LAYER interactions are found in many aeronautical applications such as air intakes or overexpanded nozzle flows. Fully separated interactions have been widely studied in the past [1–5]. Whatever the flow configuration (compressions ramps, shock reflection, blunt fin, or overexpanded nozzles), low-frequency shock motions are observed when the flow is separated, although their origin is not always clearly established [4–8]. In the case of the reflection of a shock wave on a turbulent boundary layer at a moderate Reynolds number, it has been recently proposed to relate the low-frequency motion of the leading shock (denoted “reflected shock” in Fig. 1) to the dynamics of the separated region developed downstream [6,9]. The link between the leading shock motion and the low-frequency unsteadiness was not fully specified, although some elements have been examined. For example, the relation between the low-frequency breathing of the separated region and the dynamics of the large coherent scales formed in the mixing layer originating at the foot of the leading shock has been discussed [3,6,9]. These structures produce frequencies at least one order of magnitude higher than the low-frequency shock motions. Their influence on the shock unsteadiness has still to be explored. Moreover, recent experimental investigations of various shock reflections have shown that incipient separation presents several similarities with separated cases, with evidence of low-frequency shock unsteadiness as in separated cases [6,10].

Recent work by Touber and Sandham [8] has proposed an analysis in which the response of the shock system to external perturbations is examined, providing an estimate of the low-frequency range of the interaction and justifying a former heuristic theory. This approach, however, was not well adapted to the determination of the origin of the low frequencies. The results presented here provide a quite different viewpoint. To some extent, it complements the results of [8]. From the simulation of comparable parameters, the details of the physical mechanism are explored, giving rise to the

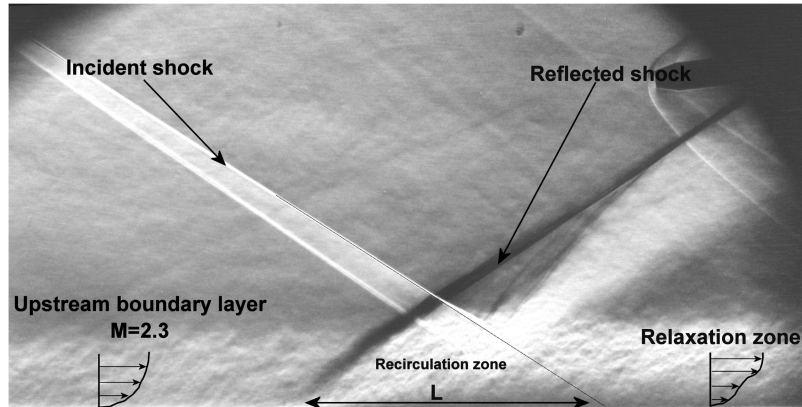


Fig. 1 Schlieren visualization of the fully separated interaction. Adapted from [6].

upstream/downstream influence on the shock motion; it also identifies spatially the zones controlling the motion of the different parts of the shock system, along with the frequency ranges that are involved. All these analyses are applied to a shock reflection configuration described in the following.

A Mach 2.3 shock reflection was set up in the Institut Universitaire des Systèmes Thermiques Industriels (IUSTI) supersonic wind tunnel. The flow deflection angle θ can be set from $\theta = 5.5$ deg to $\theta = 9.5$ deg, causing flow separation from incipient to fully separated. The organization of the flow is illustrated by a schlieren visualization of the interaction in Fig. 1. Results include (time-resolved) hot-wire measurements along the leading shock and velocity field measurements from particle image velocimetry (PIV) (not resolved in time). Details on the experimental setup and the results can be found in [3,6,9,11,12]. The Reynolds number based on the momentum thickness of the upstream boundary layer is about 5000, a convenient value to perform large-eddy simulation (LES) of such a flow. The present work complements the experimental results by bringing time-resolved data obtained from LESs of the same configuration.

The numerical method and aerodynamic parameters are described in Sec. II. The unsteadiness of the leading shock is characterized in Sec. III. As will be shown, it involves two distinct frequency bands. Each one will be related with phenomena occurring in particular regions of the flow, and the main features of the communication paths from these regions to the shock are described in Sec. IV.

II. Numerical Simulation of the Interaction

A. Computational Model and Parameters

Since the flow under study is fully turbulent with a moderate Reynolds number, and since it develops low-frequency unsteadiness, a turbulent modeling relying on the LES method appears to be a good candidate to perform time-accurate computations. As a matter of fact, LES has been proved to be a suitable modeling to resolve reflecting shock/turbulent boundary-layer interactions of the type described above. The LESs have produced accurate predictions of the mean features of the flow [13] and of the low-frequency unsteadiness, in good agreement with experiments [14].

The various computations are performed using ONERA's FLU3M solver, which has been extensively used in the recent years to analyze successfully compressible flows by either detached eddy simulation (DES), LES, or direct numerical simulation (DNS) [15–17]. The numerical scheme is designed to be able to capture the shock while meeting the LES requirement of very low dissipation in the turbulent region [18]. This is achieved by adding the dissipative part of the Roe scheme [19], modulated by Ducros et al.'s sensor [20], to a second-order centered scheme. The subgrid filtering is implicitly provided by the mesh, and the subgrid modeling relies on the selective mixed-scale subgrid model, well suited for compressible wall-bounded flows [21]. Time integration is achieved by means of a second-order-accurate implicit Gear scheme [22] with a time step of 2.5×10^{-7} s yielding maximal Courant–Friedrichs–Lowy numbers of 12 so as to

make the implicit time filtering negligible with respect to the implicit grid filtering. The resulting nonlinear system is solved iteratively at every time step with six subiterations, yielding a reduction of the residuals of 1.5 orders of magnitude at worst and more than 2.5 orders of magnitude on average.

Following [13], the computations aim at reproducing only the midspan part of the wind tunnel, excluding the influence of the sidewalls. Periodic boundary conditions are consequently used in the spanwise direction, with a spanwise extent of the computational domain equal to 1.6 boundary-layer thicknesses δ , corresponding at least to three times the expected height of the separation bubble. The domain inflow and outflow boundaries are located 10δ away of the interaction region and rely on the characteristics boundary condition.

The mesh is designed to match the resolution required to solve wall-bounded flows by LES with values $\Delta x^+ \simeq 40$, $y_1^+ \simeq 0.9$, and $\Delta z^+ \simeq 16$. The grid stretching in the vertical direction is mild in order to be able to accurately capture the recirculation bubble, yielding a number of cells located in the initial boundary-layer thickness of 95. The mesh is stretched in the streamwise direction starting from 5δ downstream of the interaction region in order to progressively damp the convected vortices. The total cell count is equal to 5.5 million. Such a moderate grid size allows a very long time integration ranging from 0.5 million to 2 million time steps, corresponding to 0.125 to 0.5 s and being large enough to resolve 50 to 150 periods of the low-frequency oscillations. These numbers of periods are comparable with or larger than values found in previous studies [5,8,18,23].

Two additional LESs of the case with the largest separation have been carried out for validation purposes. The first computation relies on a refined mesh with $\Delta x^+ \simeq 30$, $y_1^+ \simeq 0.9$, $\Delta z^+ \simeq 12$, and 105 cells spanning the initial boundary-layer thickness. The time step was reduced to 2×10^{-7} s for this simulation. The second computation is based on the same grid resolution and the same time step as the original one but with the span of the computational domain extended to 11δ . Both computations were run for 35 ms, a time large enough to obtain converged first- and second-order statistics and allowing the spectral analysis of about 10 periods of low-frequency oscillations.

Velocity, density, and pressure data over various horizontal, vertical, and transverse planes are stored on disk with a 200 kHz sampling rate, except for the computation on the refined mesh for which a 500 kHz sampling rate was set. The 200 kHz rate is not high enough to sample adequately the data in the incoming boundary-layer region for which the maximum in the pressure spectrum is located at about 70 kHz. However, comparisons between data sampled at 200 and 500 kHz demonstrate that the former rate is high enough to ensure a negligible aliasing in the interaction region. In this region, less than 5% of the total density power spuriously originates from the aliasing for every frequency in the ranges of interest, namely, the low-frequency unsteadiness and the intermediate frequencies corresponding to the large scales of the mixing layer/shedding regions.

B. Boundary Conditions

An adiabatic boundary condition is enforced at the wall, and characteristic-based boundary conditions are used at the outflow and upper boundaries. Turbulent boundary conditions at the inflow are set using a variant of the synthetic eddy method (SEM) [24,25] suited to supersonic boundary layers: the method described in [25] was modified in the following ways:

- 1) Increase by a factor of 10 the density of the synthetic eddies, yielding a more Gaussian-like probability distribution of the velocity fluctuations. This makes it possible to damp the tails of the distribution associated with fluctuations of huge kinetic energy, resulting in nonphysical high values of the local Mach number.

- 2) Add density fluctuations computed from the streamwise velocity fluctuations using the strong Reynolds analogy coupled with the linearized ideal gas law and zero pressure fluctuations so as to achieve zero mean.

- 3) Renormalize the strength of the eddy locally in order to set at the inflow exactly the wanted Reynolds stress profiles, even in regions of overlapping modes.

- 4) Use temporal characteristics to achieve nonreflectiveness of the boundary condition in the subsonic region of the boundary layer.

Following [25], five modes were distributed over the boundary-layer height, using the proposed loci, length scales, and timescales, but with Gaussian shape functions only.

It has been verified by comparisons with the experiments and with an auxiliary LES computation of a freely transitioning boundary layer that this method is able to recover accurate turbulence statistics and the expected organization within a development length smaller than $10\delta_0$. At the reference station $x = 260$ mm, located $9.5\delta_0$ downstream of the inflow and at least δ_0 upstream of the interaction region, the values of the friction velocity computed either from the derivative at the wall or using Clauser's method, differ by less than 4 and 1.5%,

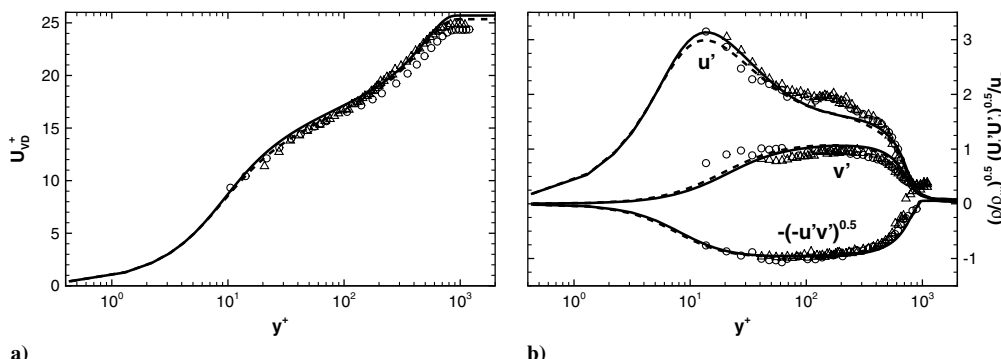


Fig. 2 Velocity profiles in the incoming boundary-layer van Driest a) transformed mean velocity profiles and b) rms velocity profiles (standard LES: solid lines; refined LES: dashed lines; experiment [26]: circles; and experiment [9]: triangles).

respectively, from the experimental values [26,27] estimated from Clauser's method. Moreover, the differences between the computations and the experiments regarding the displacement and the momentum thicknesses are lower than 2%.

These concordances can be assessed by looking at the mean and fluctuating velocity profiles plotted in the wall unit in Fig. 2. LES profiles were taken at $x = 260$ mm. Mean velocity was measured by pitot probes at $x = 260$ mm (circles), and rms velocity was measured at the same location by laser Doppler anemometry (LDA; circles). More recent experiments using LDA are also reported (triangles). They have been performed at $x = 240$ mm. These two locations correspond, respectively, in the LES to $9.5\delta_0$ and $7.4\delta_0$ from the inflow plane. Note that the slight differences seen in the van Driest velocity profiles can be almost suppressed by using Clauser's method to estimate the friction velocity from the LES data. The most noticeable discrepancy is found at the end of the log region where the streamwise fluctuations are underestimated with respect to the experiments. However, this discrepancy was also found, although slightly weakened, in the LES computation of a freely transitioning boundary layer (mentioned above). Consequently, it has not to be associated with the SEM. Lastly, the method has been found to be free of low- to medium-frequency forcing found especially for the pressure in preliminary tests [28] for which the compressible variant [29] of the Lund recycling method was used.

C. Flow Parameters

Three LESs were made to reproduce flow cases in incipient, mild, and full separation conditions, respectively, corresponding to flow deviations of 5.5, 8.0, and 9.5 deg in the experiments performed at the IUSTI. However, these shock reflection experiments were sensitive to lateral effects due to the finite span of the wind tunnel, as recently

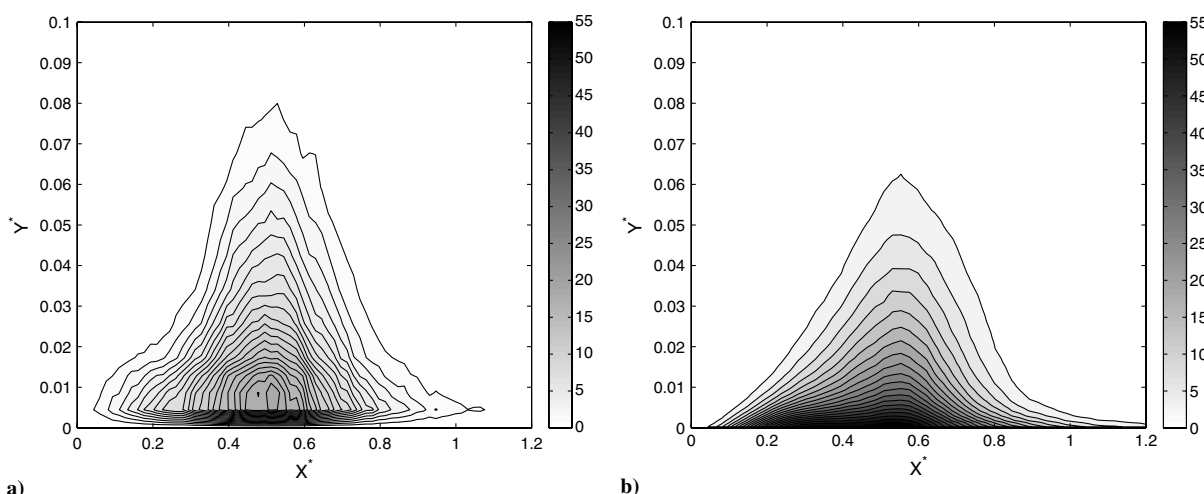


Fig. 3 Percentage of reverse flow from a) PIV measurements and b) LES data.

Table 1 Geometrical parameters of the interactions

| θ | δ , mm | L , mm | H_i , mm | H_i/δ | H_e , mm | H_e/δ |
|----------|---------------|----------|------------|--------------|------------|--------------|
| 6.3 deg | 11 | 25 | 7.5 | 0.68 | 7.5 | 0.68 |
| 8.0 deg | 11 | 38 | 12 | 1.09 | 23.5 | 2.14 |
| 9.5 deg | 11 | 63 | 21 | 1.91 | 56 | 5.09 |

shown by the RANS computations carried out for the European Unsteady Effects of Shock Wave Induced Separation project [12] and the DES by Garnier [18]. This leads to experimental sizes of interactions being up to 20% larger than the lengths found in the computations, not taking into account the sidewalls. Such differences may be of low influence on the unsteadiness for the $\theta = 8.0$ deg and $\theta = 9.5$ deg cases, since the change in size of the interaction region is not large enough to induce a change in the separation state. Therefore, computations associated with these cases are carried out for the same flow deviation angle as the experiments.

The incipient case should, on the contrary, be very sensitive to any reduction in the size of the interaction that possibly could result in changing the onset of separation. The flow deviation angle of the incipient computation has consequently been adjusted iteratively to $\theta = 6.3$ deg so as to result in an interaction length L (see Fig. 1) defined as the distance from the foot of the leading shock to the extrapolation down to the wall of the incident shock, equal to the experimental value of $L = 25$ mm found in the experiments. The flow computed from this setup exhibits a similar separation state as the experiment, as demonstrated by the distribution of the reverse flow probability plotted in Fig. 3.

Note that the interaction lengths L and some other geometrical parameters useful for further analyses are listed for the three interactions in Table 1.

D. Validation

The accuracy of the LES can first be evaluated by analyzing the sensitivity of the computations to the definition of the computational grid for the 9.5 deg case. The divergence between the standard computation, the LES carried out on a refined mesh, and the simulation with a wider span has to first be analyzed for the incoming boundary layer. No difference at all is found between the standard and the span-extended computations in that region, whereas the comparison between the standard and refined computations shows that metrics of the boundary layer, such as the friction velocity, momentum thickness, and shape factor, differ by less than 1.5% between the two simulations. Figure 2a confirms this agreement. Fluctuation profiles of Fig. 2b also collapse correctly.

When focusing on the interaction region, the standard and refined LESs exhibit the very same properties: separation length as well as interaction length differ by less than 1%, as seen in Fig. 4. Moreover, almost identical geometry of the separated region and streamwise evolution of the friction coefficient are seen in this figure. The computation with an enlarged span also shows very similar features but with lengths reduced by 2% (interaction) and 6% (separation).

This has to be associated with the rather large asymptotic values of the spanwise correlations coefficient found in some part of the interaction for the LES with the 1.68 span: $c_{uu}(\xi = 0.88) = -0.26$ close to the wall at the beginning of the separation and $c_{uu}(\xi = 0.88) = -0.17$ in the shedding region. The narrow span computation

of the 9.5 deg case appears to therefore be slightly confined. However, no other difference beyond the confinement-induced enlargement has been observed between the physics found in the narrow and wide computations. This is consistent with the analysis of one of the computations described in [8] subject to a much higher confinement. Particularly, the unsteady behavior of the interaction, as deduced from the wall pressure spectra, appears to be unaffected once normalized using L . Note that the short duration of the enlarged computation results in a noticeable level of statistical uncertainty for the spectra, but this can be counterbalanced for the most part by a space averaging in the spanwise direction.

Maximum absolute values of the streamwise correlation coefficient of velocity were found lower than 0.1 at every location of the 6.3 and 8.0 deg computed flowfields. It is therefore very unlikely that these computations are subject to spanwise confinement, and no extra computation with an extended span has been done.

A grid independence study has been carried out for 4.8 deg computations not described in this paper by using the same standard and refined grids as the 9.5 deg case. Grid convergence was fulfilled for the $\theta = 4.8$ deg case, similar to the 9.5 deg case. Consequently, it is believed that refined grids should not bring significant improvements for the 6.3 and 8.0 deg computations.

The ability of the computations to reproduce the main features of the flow unsteady behavior can be evaluated by looking at the streamwise evolution of the wall pressure spectra plotted in Fig. 5. In this figure, the spectra have been normalized by the variance of the local wall pressure. Strouhal numbers of 0.03 and 0.5 are indicated along with locations $X^* = 0$ and $X^* = 1$. All three computations, as well as the $\theta = 8.0$ deg and $\theta = 9.5$ deg experiments, exhibit a similar development of the interaction, as described in [3]: the first part of the interaction is dominated by a low-frequency component, followed by a transition region of increasing characteristic frequencies related to the development of the mixing layer that eventually result in a shedding process with an almost constant frequency, lower than the typical ones in the incoming boundary layer.

Assessment of the fidelity of the LES can be performed in a more quantitative way by normalizing both lengths and frequencies to take into account the differences between experiments and computations regarding the size of the interaction. The dimensionless coordinates $X^* = (x - X_0)/L$ and $Y^* = y/L$ are used, where X_0 is the mean position of the foot of the leading shock. In this representation, the interaction extends from $X^* = 0$ to $X^* = 1$. In separated cases, previous works [3,30] have used a nondimensional shock frequency, or Strouhal number St_L , defined as

$$St_L = \frac{f \cdot L}{U_1} \quad (1)$$

where f is the frequency, L is the interaction length, and U_1 is the velocity downstream the incident shock. It has been shown that, for Mach numbers greater than 2, separated interactions experience low-frequency shock motions around $St_L \approx 0.03$ (see [31]). Such a value is clearly seen in Fig. 5d for the experiment at $\theta = 8.0$ deg. It is recovered for the LES of the interaction with separation at $\theta = 8.0$ deg and $\theta = 9.5$ deg in Figs. 5b and 5c, although the former case exhibits peaks spread on each side of the $St_L = 0.03$ line rather than a smooth bump centered at $St_L = 0.03$. This difference is due to

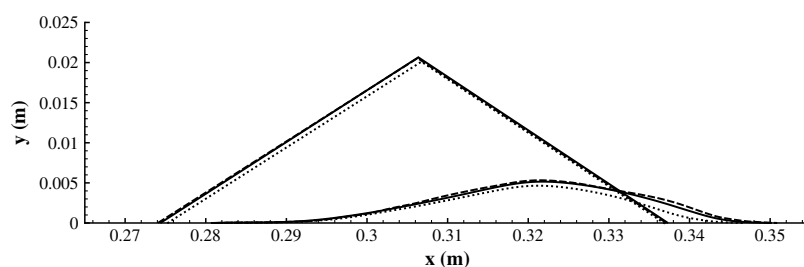


Fig. 4 Separation line and geometry of the lower part of the incident and leading shocks (see Fig. 1): standard LES (solid lines), refined LES (dashed lines), and standard LES with increased span (dotted lines).

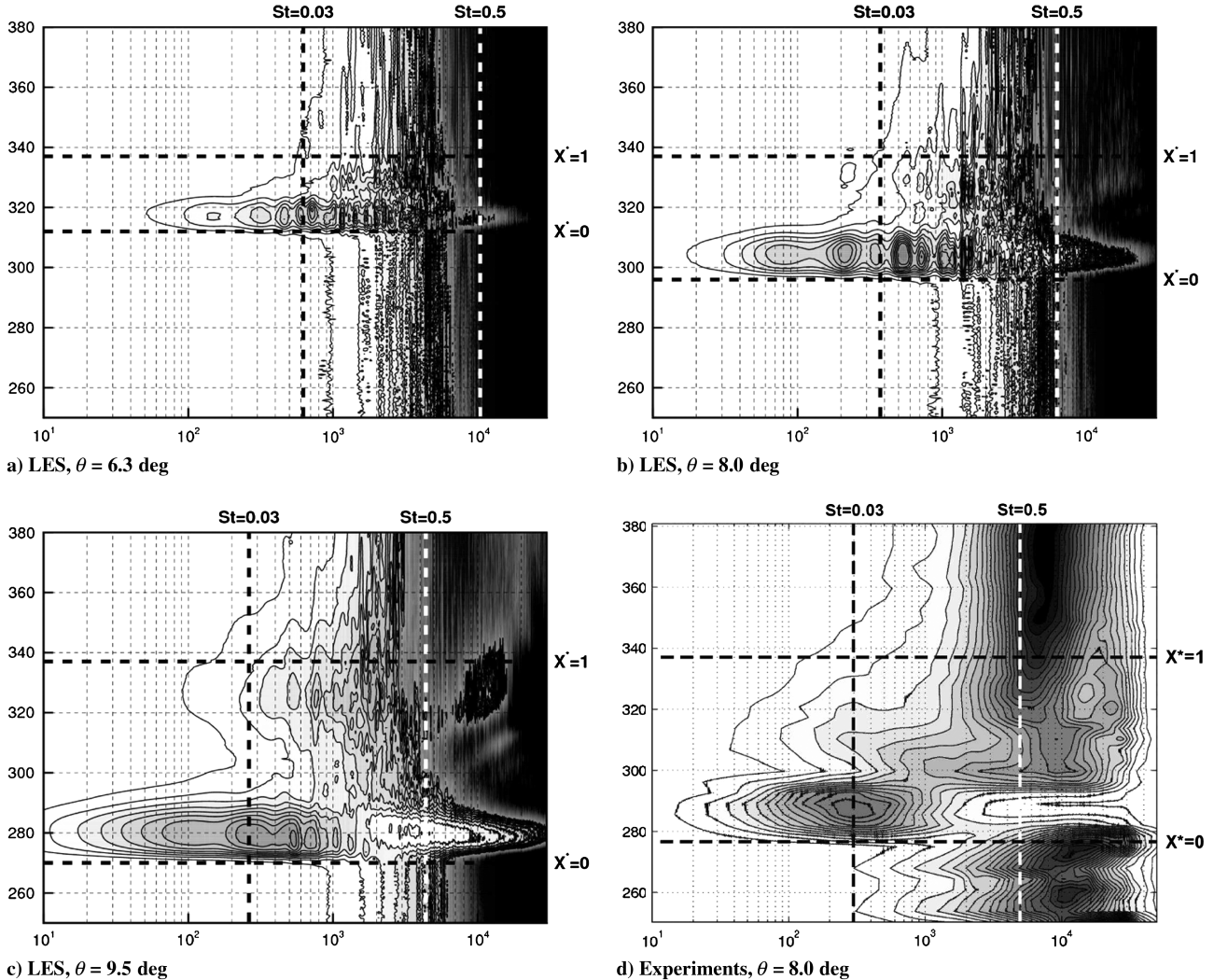


Fig. 5 Wall pressure premultiplied power spectra as a function of frequency and streamwise location (abscissa: Hz; ordinate: mm).

the rather short duration of the $\theta = 8.0$ deg computation with about 50 periods of the low-frequency shock motion, as checked by computing spectra from experimental data restricted to a similar duration that exhibit similar uneven patterns.

No such well-defined low-frequency content was found in the experimental spectra related to the incipient separation, despite evidence of energy content in this range [6,10]. This appears when looking at the premultiplied power spectrum of Fig. 6 computed by the Burg method from the time series of a hot wire located on the mean location of the leading shock at $y = 1.8\delta$. This figure compares

the spectra determined from a long time series of 10 s (experiments with $\theta = 5.5$ deg denoted by the bold solid line) and short time series of 250 ms (experiments with $\theta = 5.5$ deg denoted by the dotted line and LES with $\theta = 6.3$ deg denoted by the dashed line). The streamwise momentum premultiplied spectrum from the incipient LES computation at the same location nonetheless seems to result in a slightly noticeable bump roughly centered at $St_L = 0.03$, but this difference between experiments and computations may be again due to the difference in the temporal length of the signal. When the experimental signal is restricted to the same duration as the LES computation, spectra from the experiments and the LES show very similar features, with the exception of the highest frequencies, because of the strain gauge effect of the hot wire.

It is therefore concluded from Figs. 5 and 6 that the present LESs are able to accurately reproduce the dominant unsteady features found in the experiments while giving access to time-resolved data encompassing the whole flowfield. In the next part, the main results obtained from the LES computations will be presented, both for the mean fields as well as for the unsteady aspects.

III. Shock Motions and Regions of Influence

A. Power Spectrum of the Shock Positions

The time-resolved data are used in the first place to characterize the kinematics of the leading shock. The LES data are considered to track the position of the shock at each time. The location is determined at every time step and for every elevation by seeking the maximum of the pressure gradient in the direction normal to the shock. The premultiplied spectra of shock positions at the normalized elevation

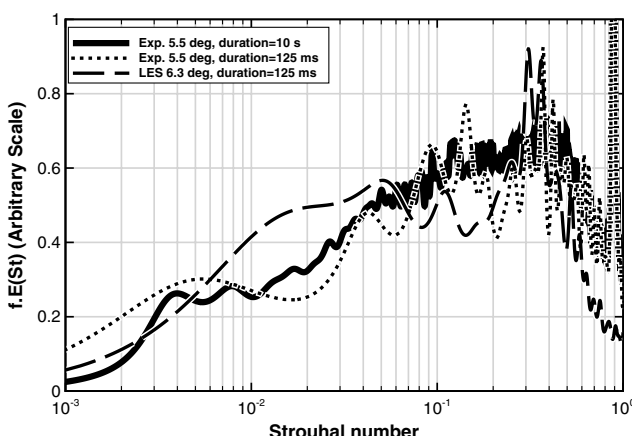


Fig. 6 Power spectra of streamwise momentum on the mean shock at elevation $y/\delta = 1.8$.

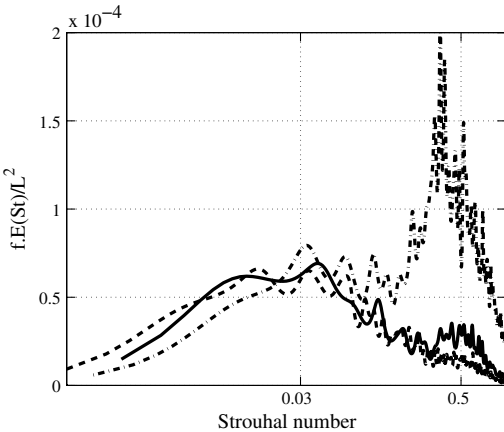


Fig. 7 Power spectra of the shock streamwise location at elevation $y/H_i = 2$.

$y/H_i = 2$, where H_i is the elevation of the crossing point of the incident and leading shocks, are plotted versus the Strouhal number in Fig. 7. Note that the premultiplied spectral density is normalized here by the square of the interaction length. The dashed-dotted line corresponds to incipient separation ($\theta = 6.3$ deg), the solid line corresponds to mild separation ($\theta = 8.0$ deg), and the dashed line corresponds to full separation ($\theta = 9.5$ deg). Here, the height H_i has been used to normalize the ordinate y . When changing the deviation angle θ , the shock angle varies so that the triangles formed by the crossing of the incident and leading shocks cannot be similar. However, in practice, as seen in Table 1, the differences are small, the pattern is almost unchanged, and normalizing by H_i or by L would lead to the same evolutions. The two frequency ranges $St_L \approx 0.03$ and $St_L \approx 0.5$ are observed with different importance. Moreover, the spectra normalized by L^2 appear to collapse at low frequencies ($St_L \approx 0.03$). This is in agreement with [3], in which it is shown that the measured length of the leading shock excursion varies roughly like the length of interaction. As this amplitude of the shock motion is closely related to the low frequencies, the observed collapse of the spectra when normalized by L^2 is not surprising. This suggests still more firmly that L is the pertinent length scale for these low-frequency motions, leading to self-similar behavior in this frequency range.

Low-frequency unsteadiness is expected in the separated case. However, it is more surprising to find it also in the incipient case at the same Strouhal number. In previous work, the same characteristic low and intermediate Strouhal numbers were observed in the interactions for separated cases [3]. They have been, respectively, related to some breathing of the separation bubble and to the development of vortical structures of Kelvin–Helmholtz type in the mixing layer downstream of the separation shock [3,6]. The former physics was energy-dominant. In the incipient case, it seems that identical sources of unsteadiness are found but in different proportions: the shock motion associated with the intermediate frequencies prevails. Nevertheless, the normalizing of the displacement at low frequencies by the interaction length yields the same amplitude as in the separated cases. The origin of both low- and intermediate-frequency shock motions will be discussed in the next sections.

B. Correlation Fields in the Interaction

The pressure fields are now considered to investigate where the characteristic frequencies $St_L \approx 0.03$ and $St_L \approx 0.5$ are present in the field and how they can influence the leading shock motions. Two pressure correlation fields have been computed, associated with the two characteristic frequencies. They are derived from the following procedure:

- 1) First, the pressure fluctuations of the whole flowfield and the time series of the streamwise location of the shock at a given elevation are bandpassed around the considered frequencies, with a bandwidth of $0 \leq St_L \leq 0.1$ for the low-frequency range and of $0.3 \leq St_L \leq 0.8$ for the intermediate-frequency range.

- 2) Then, the cross correlations between pressures and the shock streamwise location at the selected elevation are computed.

This procedure has been applied for the three interactions under consideration, and the results are plotted in Figs. 8a–8f. The elevation at which the streamwise location of the shock is extracted is marked by a star. A dashed line denoting the sonic line and a dashed-dotted line denoting the leading shock have been added to these figures for the sake of clarity.

Figure 8c presents the fields of the resulting cross-correlation coefficients in the low-frequency range for the mildly separated interaction ($\theta = 8.0$ deg). The coefficients have been computed by taking as reference the shock motion at elevation $y/H_i = 1.4$ for practical reasons. Note, however, that the results were found insensitive to the location along the shock. Figure 8c puts in evidence a high level of correlation between the shock and the initial part of the interaction, whereas the expansion wave, the second part of the interaction, and the downstream flow are in anticorrelation with the shock position. Similar results were already obtained for shock reflection, as well as for the compression ramp from experimental [1,3,32,33] as well as numerical [7,28] unsteady wall pressure data. They are now generalized in the whole field of the interaction. It can be seen in Figs. 8a and 8e that similar properties are also found for the $\theta = 6.3$ deg and $\theta = 9.5$ deg flow deviations, respectively.

Results obtained for intermediate frequencies are shown in Figs. 8b, 8d, and 8f. In all cases, the value of y/H_i has been set large enough to have signals not directly polluted by the fluctuations of the shear layer. This led to the value of $y/H_i = 3$ for the incipient case and for the 8.0 deg deviation. In the 9.5 deg case, it was not possible to reach such high values because of the smaller relative extent of the computational domain; a compromise at $y/H_i = 1.8$ was adopted to minimize the contribution of the turbulent layers. Moreover, the results are weakly sensitive to the choice of y/H_i . When focusing on the mild separation case $\theta = 8.0$ deg in Fig. 8d, two distinct periodic patterns are observable. The first pattern is found along the leading shock, while the second pattern is located downstream of the foot of the expansion wave and spans the vortex shedding region ($X^* \gtrsim 0.7$). More detailed information on these patterns can be gained by looking at the incipient and fully separated cases.

Considering the $\theta = 6.3$ deg incipient case, Fig. 8b provides the visualization of a large part of the leading shock located above the crossing point with the incident shock located at elevation $y/H_i = 1$. Consequently, the alternated correlated and anticorrelated regions found along the leading shock in Fig. 8d are more clearly seen here. They are, on the contrary, barely seen in Fig. 8f, corresponding to the $\theta = 9.5$ deg case, since they are mostly located above the domain on which the unsteady data have been sampled.

The second correlation pattern, located in the shedding region downstream of $X^* \approx 0.7$, is also found for both the incipient and fully separated cases in Figs. 8b and 8f, respectively. Note that the wavelength does not scale with L , ranging from $\lambda \approx 1.7L$ for the incipient case to $\lambda \approx 1.1L$ for the fully separated case. This is due to both an increase in the Strouhal numbers and a decrease in the convective velocity of the shed vortices in region $0.8 \lesssim X^* \lesssim 2$ when θ is increased. Furthermore, the pattern extends further upstream into the mixing layer region for the fully separated case. The wavelength is slightly lower in that region. This is in rather good agreement with the value determined experimentally from two-point wall pressure measurements that were associated with the mixing layer structures [3].

It consequently appears that the cross-correlation pattern found at the end of the mixing layer and in the shedding region is directly related to convected vortices. The nature of the pattern found along the leading shock is, however, less clear and further analyses are required to clarify that point.

C. Propagation and Convection Velocities in the Interaction

1. Convective Velocity of Vortical Structures in the Mixing Layer

In previous experimental works, two-point measurements of unsteady wall pressure have been performed. Evidences of links

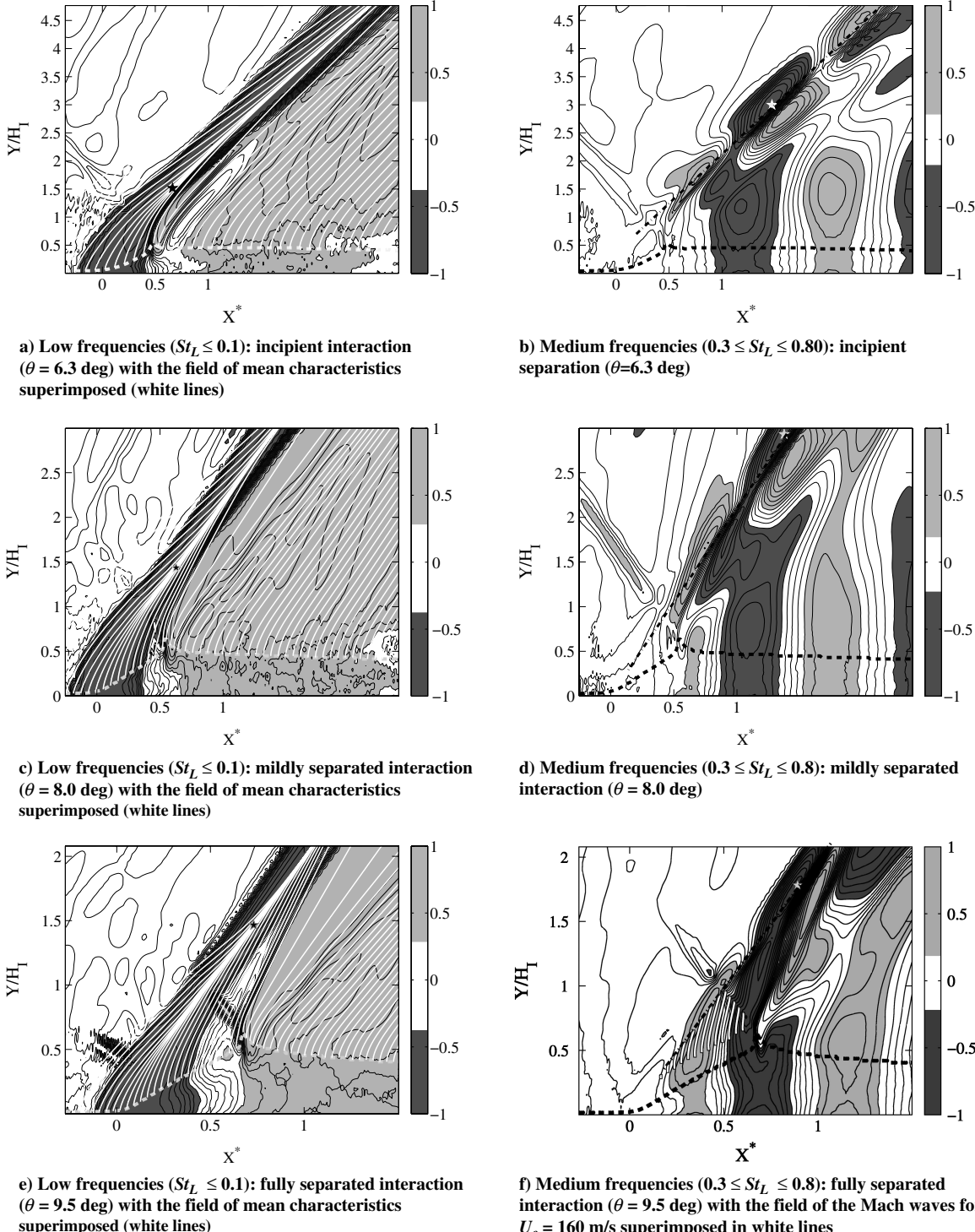


Fig. 8 Maps of bandpassed cross correlation between pressure and time series of the streamwise location of shock.

were found between the leading shock and the other regions of the interaction, depending on the frequency range [3]. Typical convection velocities were determined and associated with each frequency domain.

At low frequency, no convective behavior was found in the interaction, except for the 9.5 deg case, within a small region in the vicinity of the reattachment point [33].

The intermediate frequencies have a convective behavior. In the region $0.2 \lesssim X^* \lesssim 0.5$, phase velocities deduced from wall pressure measurements were found to be rather insensitive to the value of the deviation angle θ , with a typical value of 170 m/s. This value was associated with the convective velocities U_c of the structures in the mixing layer [3].

These experimental results have been confirmed by considering the unsteady wall pressure data computed by LES. Moreover, LESs give access to unsteady data over the whole flowfield, allowing a more direct evaluation of U_c by using phase velocities deduced from velocity measurement along the centerline of the mixing layer. Convective velocities ranging roughly from 160 m/s for the fully separated case to 200 m/s for the incipient case are obtained, in good agreement with previous values.

2. Disturbance Propagation Along the Leading Shock at the Intermediate Frequencies

LES data were also used to compute the propagation velocity V_p associated with the corrugation of the shock. Time delays τ_{opt}

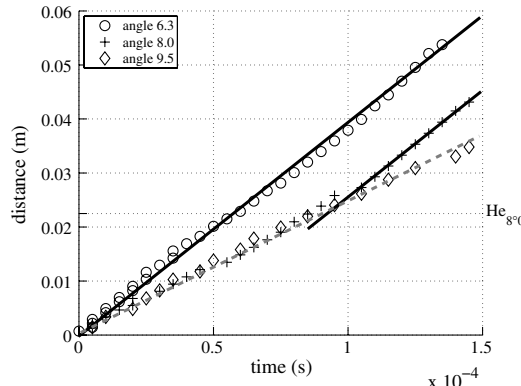


Fig. 9 Separation distance ξ vs optimal time delay τ_{opt} along the shock [\circ : incipient separation ($\theta = 6.3$ deg); $+$: mild separation ($\theta = 8.0$ deg); \diamond : full separation ($\theta = 9.5$ deg)].

optimizing the cross correlation of the shock location between two points taken along the leading shock separated by a distance (ξ) have been determined. The reference point is located just above the crossing point of the two shocks, whereas the second point is placed at higher altitudes, along the leading shock. Time delays are then converted into propagation velocity V_p by the relation

$$V_p = \frac{\xi}{\tau_{\text{opt}}} \quad (2)$$

The optimum delay times for intermediate frequencies ($0.3 < St_L < 0.8$) along the leading shock have been evaluated for the three interaction intensities. They are reported in Fig. 9. The local velocity of propagation along the shock is equal to the local slope of the curve $\xi(\tau_{\text{opt}})$. Black solid lines and a gray dotted line corresponding, respectively, to velocities equal to 400 and 250 m/s have been added to Fig. 9 as references. Several behaviors can be observed, depending on the state of separation and on the distance from the reference point:

1) For the incipient separation case ($\theta = 6.3$ deg), the expansion fan is merged with the leading shock (see [9]). The propagation velocity along the shock is found approximately equal to 400 m/s.

2) For the strongest shock intensity ($\theta = 9.5$ deg), the expansion wave intersects the leading shock outside of the computational domain. The region below the intersection point H_e of the leading shock and the expansion fan has a nearly constant convection velocity of about 250 m/s.

3) For the shock of intermediate intensity ($\theta = 8.0$ deg), the computational domain is such that it is possible to evaluate the propagation velocity in both regions: below and above the intersection of the expansion fan with the leading shock. In the first region, between the shock crossing and the intersection with the expansion, the convection velocity is the same as in the $\theta = 9.5$ deg case (250 m/s), while above this region, where the leading shock and

the expansion collapse, the same convection velocity as in the incipient case is obtained (400 m/s).

To summarize, the shock kinematics at intermediate frequencies can be split into two parts on each side of the crossing point H_e . The propagation velocity of disturbances along the first part of the shock (below H_e) is about 250 m/s, while along the second part (above H_e), the propagation velocity is different and has a value about 400 m/s. The possibility of a link between these two different velocities and the kinematics of the vortical structures found in the mixing layer and in the shedding region will be analyzed in the next section.

IV. Pressure Disturbance Propagation Within the Flow

A. Reminders About Characteristics and Disturbance Propagation

An attempt will be made to interpret some of the previous results in terms of characteristic directions. This is often possible in flows with pressure gradients, since in turbulent flows, even in supersonic conditions, outside of the viscous sublayer, the pressure force is larger than friction. Therefore, outside of this thin viscous zone, the equations of motion reduce to Euler equations.

Under the assumption of an inviscid and supersonic flow, the hyperbolic equations governing compressible flows can be recast into the characteristic form. In this case, pressure fluctuations propagate along the characteristic lines, which are known as Mach waves. Shock waves are located at the coalescence of such lines. Therefore, the directions and the speed of transmission of information described in the previous sections will be compared with the properties of characteristic directions.

Such analyses are carried out by considering the mean flowfield and are consequently invalid for the high-frequency range. The upper limit of validity can be estimated to $St_L \ll 1$, as shown in the Appendix. Interpretation of the data based on this model will therefore be meaningful for the $St_L \simeq 0.03$ frequency range. It is also expected that it will help in analyzing the flow kinematics at intermediate frequencies $St_L \simeq 0.5$, although in that range, extra care will have to be taken to validate the results.

Different paths of propagation for pressure disturbances are possible. Simple cases are considered here. If the source of perturbation is stationary in a flow at velocity U , the wavefront grows at a speed equal to the sound speed C and is convected at the speed U . It is known that it remains inside of a Mach cone, or dihedral in two dimensions, and the disturbance follows a characteristic line of slope α given by

$$\alpha = \sin^{-1}(C/U) \quad (3)$$

where U and C denote the flow velocity and the speed of sound, respectively. Note that the propagation of the disturbance results from the motion of the tangency point of the wavefront represented in simple cases by the sphere or the circle convected at velocity U and growing at a rate equal to sound speed, as sketched in Fig. 10a. In

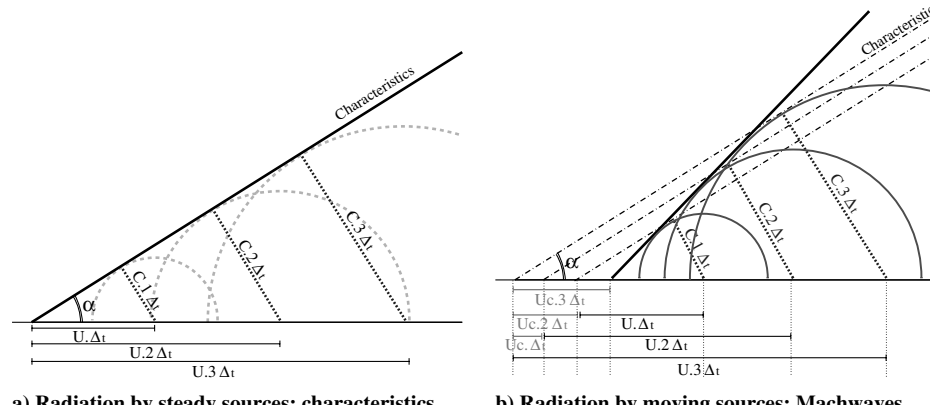


Fig. 10 Propagation of pressure disturbances.

such conditions, the propagation velocity U_η along this characteristic is equal to

$$U_\eta = \sqrt{U^2 - C^2} \quad (4)$$

Taking into account the fact that, for the present cases, the angle between the characteristic lines and the shock is rather small, the propagation speed V_{Pc} of the disturbance along the shock can be approximated by

$$V_{Pc} \simeq U_\eta \quad (5)$$

When the source of perturbation moves with velocity U_c , radiation should be considered in a frame of reference moving at velocity U_c . Such sources consequently radiate Mach waves of slope α' :

$$\alpha' = \sin^{-1} \left(\frac{C}{U - U_c} \right) = \sin^{-1} \left(\frac{1}{M_c} \right) \quad (6)$$

where M_c is the convective Mach number; see, for example, [34]. This is illustrated by Fig. 10b.

Some comments can be made on this figure. At time $t = 0$, a perturbation is produced at the origin. The situation is examined at time $3\Delta t$ in the example given in Fig. 10b, for which the wavefront has traveled over a distance $3\Delta t U$, and its radius is $3\Delta t C$. Perturbations produced at intermediate times Δt and $2\Delta t$ are considered, with their properties at time $3\Delta t$. After a time Δt , the source has moved along a distance $\Delta t U_c$. As we consider the situation at time $3\Delta t$, the wavefront has traveled over a distance $2\Delta t U$, and its radius is $2\Delta t C$. For a perturbation emitted at time $2\Delta t$, the reasoning is the same and corresponds to the third circle of radius $\Delta t C$, in Fig. 10b. Simple geometrical similarity considerations show that the envelope of the wavefronts (Mach wave) is a straight line of slope α' , defined in Eq. (6).

In this case of moving sources, disturbances propagate along the Mach waves with a speed U_ζ given by the companion relation of formula (4):

$$U_\zeta = \sqrt{(U - U_c)^2 - C^2} \quad (7)$$

Moreover, when the Mach wave produced by such a convected structure intersects the shock wave of angle σ with respect to the direction of convection, the propagation speed $V_{P_{MW}}$ of the disturbance along the shock is equal to

$$V_{P_{MW}} = U_c \left(\frac{\sin(\alpha')}{\sin(\alpha' - \sigma)} \right) \quad (8)$$

Note that the two previous relations are obtained for \mathbf{U} and \mathbf{U}_c being collinear. It has been checked that this condition holds approximately for the present flow cases.

Geometrical and kinematical properties of the disturbance propagations described by Eqs. (3–8) are summarized in Fig. 11. It is obvious from this figure that steady and convective sources radiate in different directions. Consequently, this general framework will be used in the next sections to seek for the sources located within the

interaction region that could be responsible for the propagation of perturbation along the leading shock.

B. Regions of Influence for the Shock Unsteadiness at Low Frequencies

As already mentioned, no convective properties were found over the low-frequency range for the most part of the interaction region [3]. Consequently, the domain of influence of the low-frequency unsteadiness has, rather, to be searched for by considering the characteristics. This domain is visualized in Fig. 8a for the 8.0 deg interaction by plotting the field of mean characteristic. As seen on this figure, the isolines of cross correlation closely follow the characteristic lines. The regions of origin for the disturbance along the shock at low frequency can therefore be identified as follows:

1) The region of the leading shock located below H_e is affected by disturbances coming from the first part of the separated zone $0 < X^* < 0.5$.

2) The kinematics of the region above H_e is governed by disturbance sources located at the foot of the expansion fan with $X^* \simeq 0.6 - 0.7$.

It appears, consequently, that the low-frequency motion of the whole leading shock has to be associated with the low-frequency motion of the separation bubble and/or of the interaction zone. This result seems to hold for the fully separated case $\theta = 9.5$ deg in Fig. 8e, but also, more surprisingly, for the incipient case $\theta = 6.3$ deg, although only in the $y \geq H_e$ region because of the evanescence of the $y < H_e$ region in this case, as seen in Fig. 8a.

C. Regions of Influence for Shock Unsteadiness at Intermediate Frequencies

1. Leading Shock Below the Expansion Fan

Different values of the propagation velocity V_p of the disturbances along the leading shock have been found in Sec. III.C.2 on each side of the intersection point H_e with the expansion fan. It suggests that the physics responsible for propagation differs from one part of the leading shock to the other. It is therefore reasonable to assume that the location of the disturbance sources may also differ. The region of the leading shock located below H_e will be analyzed first, and the analysis will focus on data from the $\theta = 9.5$ deg case that bring forth the largest extension of this region.

The cross-correlation map in Fig. 8f shows that the fluctuations along the lower part of the leading shock are correlated with fluctuations located within the region associated with the development of the mixing layer $0 \lesssim X^* \lesssim 0.5$. An almost constant convection velocity $U_c \simeq 160$ m/s has been associated with this region in Sec. III.C.1. Therefore, Mach wave radiation computed from the same convection velocity radiation has to be considered.

The path followed by a Mach wave radiation can be obtained by the integration of Eq. (6) over regions where $M_c \geq 1$. Such paths have been superimposed to the cross-correlation map of Fig. 8f. This figure shows a good concordance between the radiation paths and the isolines of correlation. Mach wave radiations emitted by the vortical structures of the mixing layer could therefore be responsible for the disturbances found along the leading shock below H_e .

The velocity $V_{P_{MW}}$ induced on the leading shock by such radiations has to be computed to confirm that point. Injection of values $U = 490$ m/s and $C = 270$ m/s, typical of the region located above the edge of the mixing layer, into Eq. (6) yields $\alpha' \simeq 55$ deg. Moreover, the angle between the leading shock and the floor can be estimated to 34 deg, whereas the angle between the mixing layer and the floor is roughly equal to 12 deg, leading to $\sigma \simeq 22$ deg. The use of Eq. (8) then results in the estimation $V_{P_{MW}} \simeq 240 \pm 10$ m/s when taking into account the uncertainties on the estimation of the various angles. The same analysis can be conducted on the $\theta = 8.0$ deg case and leads to the same value, despite a slightly higher level of uncertainty due to the rather small extension of the region of the shock below H_e .

The value $V_{P_{MW}} \simeq 240$ m/s is in very good agreement with the value $V_p \simeq 250$ m/s measured from two-point two-time cross correlations on the lower part of the leading shock in Sec. III.C.2 for both the $\theta = 8.0$ deg and $\theta = 9.5$ deg cases. One may consequently

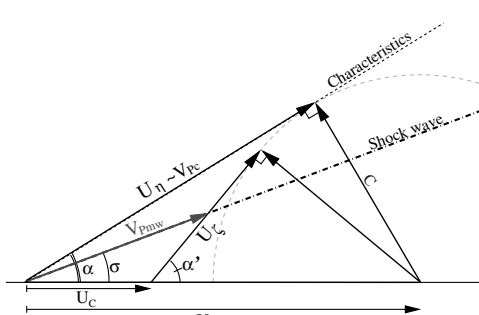


Fig. 11 General scheme for characteristics and Mach waves.

infer with reasonable confidence that the disturbances propagating along the leading shock up to H_e are induced by Mach wave radiations from the vortical structures of the mixing layer. This scheme is supported by pseudoschlieren movies computed from the LES data showing pressure waves emitted in the mixing layer region and propagated up to the lower part of the leading shock.

2. Leading Shock Above the Intersection with the Expansion Fan

Performing the same analyses as in the previous section leads to the conclusion that Mach waves radiated from the mixing layer region are not able to cross the leading shock above its intersection H_e with the expansion fan. Other possible sources for Mach waves can be looked for: for example, sources located further downstream in the vortex shedding region $X^* \geq 0.7$. A difficulty arises: the convection velocity of the vortical structures is far from being constant in that region: for instance, there is a 20% increase between $X^* = 1$ and $X^* = 3$ for the $\theta = 6.3$ deg incipient case. This results in a noticeable level of uncertainty in the definition of the paths followed by the Mach waves possibly radiated from the shed vortices.

These paths nonetheless agree well with the correlation patterns of the shedding region at intermediate frequencies seen in Fig. 8b–8f, demonstrating the relevancy of the computation. Mach waves appear not to be able to induce disturbances on the leading shock. Moreover, the resulting propagation velocity along the leading shock above H_e would be estimated at $V_{P_{MW}} \simeq 290 \pm 15$ m/s for the $\theta = 6.3$ deg case and $V_{P_{MW}} \simeq 260 \pm 10$ m/s for the $\theta = 8.0$ deg case. Both values are far from the value of the sole value $V_p \simeq 400$ found in Sec. III.C.2 for both cases. Consequently, Mach wave radiation associated with shed vortices is probably not responsible for disturbance propagation.

One has to therefore consider disturbance propagating from steady sources despite the fact that the intermediate-frequency range is rather convective in nature. The propagation velocity induced by steady sources is estimated by Eq. (5) to $V_{P_c} = 425$ m/s and $V_{P_c} = 415$ m/s for the $\theta = 6.3$ deg and $\theta = 8.0$ deg cases, respectively. These values agree reasonably with the value of V_p measured above H_e , but an admissible process based on steady sources taking origin from a mostly convective physics remains to be described.

All characteristic lines that could induce disturbances on the upper part of the leading shock originate from the foot of the expansion fan, as seen in Figs. 8a, 8c, and 8e. It has been observed in movies computed from LES data passbanded around $St = 0.5$ that this narrow region is very strongly modulated by the shedding of the vortical structures at the end of the mixing layer. It is then inferred that these almost periodic modulations may act as a stationary source of pressure fluctuations, which then propagate along the characteristics of the expansion fan.

This scenario implies that the frequency/Strouhal number of the shedding and the frequency/Strouhal number of the disturbances found along the leading shock are equal. The value of the Strouhal number St_{L_p} associated with the shock disturbances can be computed by

$$St_{L_p} = \frac{V_p L}{\lambda_p U_1} \quad (9)$$

where λ_p is the wavelength of the disturbances. The value of λ_p above H_e can be accurately inferred only for the incipient case because of the restricted size of the sampling domain. It reads $\lambda_p = 47$ mm, yielding $St_{L_p} = 0.41$ through Eq. (9). This is in acceptable agreement with the $St_L \simeq 0.5$ value associated with the shedding process [3] when taking into account the rather large uncertainty on the St_L measurement in the shedding region because of the turbulent nature of the interaction. The postulated scenario appears to therefore be plausible.

V. Conclusions

The unsteady behavior of a shock reflection on a turbulent boundary layer at Mach number 2.3 has been investigated using

results of LESs. Several cases have been computed, ranging from incipient to full separations. The computations have been carefully compared with experiments, with a special emphasis put on the unsteadiness of the interaction region. The longtime computation led to wall pressure spectra with good statistical convergence from which low- and intermediate-frequency bands have been put in evidence, whatever the state of separation. The corresponding Strouhal numbers of about 0.03 and 0.50 are similar to the experimental values [3].

These two frequency bands are also found when the spectra of the shock location are considered. The respective proportion of the energy content associated with these two bands varies with the state of separation. It is, however, demonstrated that a normalization based on the interaction length L results in a collapse of all the spectra in the low-frequency range for all separation states, from incipient to fully separated. For the intermediate-frequency range, perturbation of the shock location propagates along the shock, with propagation velocities depending on the region under consideration.

Joint analysis of the shock location-pressure cross-correlation maps and of the fields of characteristics and Mach waves leads to an identification of the sources inducing the motion of the leading shock. The displacement of the shock at low frequency is associated with the fluctuations of the interaction bubble, whereas the motions at intermediate frequency are produced by the large vortical structures of the mixing layer. The analysis of the propagation of the perturbations along the characteristics and Mach waves has led to an analytical determination of velocities in agreement with the different propagation velocities obtained along the leading shock at intermediate frequency.

The kinematics of the leading shock is split into two parts, depending on the location with respect to the crossing point between the shock wave and the expansion fan:

1) The first part is affected at low frequency by the motion of the beginning of the interaction region and at intermediate frequency by Mach wave radiation from the vortical structures produced by the mixing layer.

2) The second part of the shock is affected by disturbances issued from the foot of the expansion fan for both the low- and intermediate-frequency bands. These disturbances are associated with the breathing of the interaction region for the low-frequency range. At intermediate frequencies, the disturbances are created by the crossing of vortical structures shed from the mixing layer.

In conclusion, the shock kinematics seems to be only the mirror of the physical phenomena localized in the separated zone, whatever the frequency range.

Appendix

It is possible to underline particular properties of low frequencies and to relate them to the mean field. Let us consider the continuity equation written for density and velocity fluctuations using Favre's averaging (the analysis could also be made on momentum equations and would lead to the same conclusions):

$$\frac{\partial \rho'}{\partial t} + \tilde{u}_j \frac{\partial \rho'}{\partial x_j} + \rho' \frac{\partial \tilde{u}_j}{\partial x_j} + \frac{\partial \bar{\rho} u_j''}{\partial x_j} + \frac{\partial \bar{\rho}' u_j''}{\partial x_j} = 0 \quad (A1)$$

We want to compare the first two terms of Eq. (A1) using a decomposition of the form $\rho' = \hat{\rho} \exp[i(\mathbf{k} \cdot \mathbf{x} - \omega t)]$. The first term becomes $-i\omega\rho'$, while the second reads $i\tilde{u}_j k_j \rho'$. The time derivative term can therefore be neglected if

$$|\omega| \ll |k_j \tilde{u}_j| \quad (A2)$$

or by recasting Eq. (A2) with frequency f and using U_1 and L as typical velocity and length scales in the interaction region:

$$\frac{fL}{U_1} \ll 1 \Leftrightarrow St_L \ll 1 \quad (A3)$$

The conclusion is that, for $St_L \ll 1$, the equations of motion reduce to the steady Euler equations; therefore, pressure perturbations follow the characteristics defined by the mean field.

Acknowledgments

This work was granted access to the high-performance computing resources of Institut du Développement et des Ressources en Informatique Scientifique under the allocation 2009-021877 made by Grand Equipment National de Calcul Intensif.

References

- [1] Dolling, D. S., "Fifty Years Of Shock-Wave/Boundary-Layer Interaction Research: What Next?," *AIAA Journal*, Vol. 39, No. 8, Aug. 2001, pp. 1517–1531.
doi:10.2514/2.1476
- [2] Beresh, S. J., Clemens, N. T., and Dolling, D. S., "Relationship Between Upstream Turbulent Boundary Layer Velocity Fluctuations and Separation Shock Unsteadiness," *AIAA Journal*, Vol. 40, No. 12, Dec. 2002, pp. 2412–2422.
doi:10.2514/2.1609
- [3] Dupont, P., Haddad, C., and Debièvre, F. J., "Space and Time Organization in a Shock Induced Boundary Layer," *Journal of Fluid Mechanics*, Vol. 559, 2006, pp. 255–277.
doi:10.1017/S0022112006000267
- [4] Ganapathisubramani, B., Clemens, N. T., and Dolling, D. S., "Effects of Upstream Coherent Structures on Low-Frequency Motion of Shock-Induced Turbulent Separation," 45th AIAA Aerospace Sciences Meeting and Exhibit, Reno, NV, AIAA Paper 2007-1141, Jan. 2007.
- [5] Wu, M., and Martin, M. P., "Analysis of Shock Motion in Shockwave and Turbulent Boundary Layer Interaction Using Direct Numerical Simulation Data," *Journal of Fluid Mechanics*, Vol. 594, Jan. 2008, pp. 71–83.
doi:10.1017/S0022112007009044
- [6] Piponnaiu, S., Dussauge, J. P., Debièvre, J. F., and Dupont, P., "A Simple Model for Low-Frequency Unsteadiness in Shock-Induced Separation," *Journal of Fluid Mechanics*, Vol. 629, 2009, pp. 87–108.
doi:10.1017/S0022112009006417
- [7] Touber, E., and Sandham, N. D., "Oblique Shock Impinging on a Turbulent Boundary Layer: Low-Frequency Mechanisms," 38th AIAA Fluid Dynamics Conference, Seattle, WA, AIAA Paper 2008-4170, June 2008.
- [8] Touber, E., and Sandham, N. D., "Low-Order Stochastic Modelling of Low-Frequency Motions in Reflected Shock-Wave/Boundary-Layer Interactions," *Journal of Fluid Mechanics*, Vol. 671, 2011, pp. 417–465.
doi:10.1017/S0022112010005811
- [9] Dupont, P., Piponnaiu, S., Sidorenko, A., and Debièvre, J. F., "Investigation by Particle Image Velocimetry Measurements of Oblique Shock Reflection with Separation," *AIAA Journal*, Vol. 46, No. 6, June 2008, pp. 1365–1370.
doi:10.2514/1.30154
- [10] Souverein, L. J., Van Oudheusden, B. W., Scarano, F., and Dupont, P., "Application of a Dual-Plane Particle Image Velocimetry (Dual-PIV) Technique for the Unsteadiness Characterization of a Shock Wave Turbulent Boundary Layer Interaction," *Measurement Science and Technology*, Vol. 20, No. 7, July 2009, Paper 074003.
doi:10.1088/0957-0233/20/7/074003
- [11] Souverein, L. J., Dupont, P., Debièvre, J.-F., Van Oudheusden, B. W., and Scarano, F., "Effect of Interaction Strength on Unsteadiness in Shock-Wave-Induced Separations," *AIAA Journal*, Vol. 48, No. 7, 2010, pp. 1480–1493.
doi:10.2514/1.J050093
- [12] Doerffer, P., Hirsch, C., Dussauge, J.-P., Babinsky, H., and Barakos, G. N. (eds.), *Unsteady Effects of Shock Wave Induced Separation*, Springer, New York, 2010, pp. 287–311.
- [13] Garnier, E., Sagaut, P., and Deville, M., "Large-Eddy Simulation of the Shock/Boundary Layer Interaction," *AIAA Journal*, Vol. 40, No. 10, 2002, pp. 1935–1944.
doi:10.2514/2.1552
- [14] Touber, E., and Sandham, N. D., "Comparison of Three Large-Eddy Simulations of Shock-Induced Turbulent Separation Bubbles," *Shock Waves*, Vol. 19, No. 6, Dec. 2009, pp. 469–478.
doi:10.1007/s00193-009-0222-x
- [15] Deck, S., and Thorigny, P., "Unsteadiness of an Axisymmetric Separating-Reattaching Flow: Numerical Investigation," *Physics of Fluids*, Vol. 19, 2007, Paper 065103.
doi:10.1063/1.2734996
- [16] Simon, F., Deck, S., Guillen, P., Sagaut, P., and Merlen, A., "Numerical Simulation of the Compressible Mixing Layer Past an Axisymmetric Trailing Edge," *Journal of Fluid Mechanics*, Vol. 591, 2007, pp. 215–253.
doi:10.1017/S0022112007008129
- [17] Riou, J., Garnier, E., and Basdevant, C., "Compressibility Effects on the Vortical Flow Over a 65 deg Sweep Delta Wing," *Physics of Fluids*, Vol. 22, No. 3, 2010, Paper 035102.
doi:10.1063/1.3327286
- [18] Garnier, E., "Stimulated Detached Eddy Simulation of Three-Dimensional Shock/Boundary Layer Interaction," *Shock Waves*, Vol. 19, No. 6, Dec. 2009, pp. 479–486.
doi:10.1007/s00193-009-0233-7
- [19] Roe, P. L., "Approximate Riemann Solvers, Parameter Vectors, and Difference Schemes," *Journal of Computational Physics*, Vol. 43, No. 2, 1981, pp. 357–372.
doi:10.1016/0021-9991(81)90128-5
- [20] Ducros, F., Ferrand, V., Nicoud, F., Weber, C., Darracq, D., Gachereau, C., and Poinsot, T., "Large-Eddy Simulation of the Shock/Turbulence Interaction," *Journal of Computational Physics*, Vol. 152, No. 2, 1999, pp. 517–549.
doi:10.1006/jcph.1999.6238
- [21] Lenormand, E., Sagaut, P., Ta Phuoc, L., and Comte, P., "Subgrid-Scale Models for Large-Eddy Simulation of Compressible Wall Bounded Flows," *AIAA Journal*, Vol. 38, No. 8, 2000, pp. 1340–1350.
doi:10.2514/2.1133
- [22] Gear, C. W., *Numerical Initial Value Problems in Ordinary Differential Equations*, Prentice-Hall, Upper Saddle River, NJ, 1971, pp. 209–223.
- [23] Morgan, B., Kawai, S., and Lele, S. K., "A Parametric Investigation of Oblique Shock/Turbulent Boundary Layer Interaction Using LES," AIAA Paper 2011-3430, 2011.
- [24] Jarrin, N., Benhamadouche, S., Laurence, D., and Prosser, R., "A Synthetic-Eddy Method for Generating Inflow Conditions for LES," *International Journal of Heat and Fluid Flow*, Vol. 27, 2006, pp. 585–593.
doi:10.1016/j.ijheatfluidflow.2006.02.006
- [25] Pamiès, M., Weiss, P. E., Garnier, E., Deck, S., and Sagaut, P., "Generation of Synthetic Inflow Data for Large-Eddy Simulation of Spatially Evolving Wall-Bounded Flows," *Physics of Fluids*, Vol. 21, No. 4, 2009, Paper 045103.
doi:10.1063/1.3103881
- [26] Laurent, H., "Turbulence D'Une Interaction Onde de Choc-Couche Limite sur Paroi Plane Adiabatique ou Chauffée," Ph.D. Thesis, Aix-Marseille II Univ., Marseille, France, 1996.
- [27] Dupont, P., Piponnaiu, S., Sidorenko, A., and Debièvre, J. F., "Investigation By Particle Image Velocimetry Measurements of Oblique Shock Reflection With Separation," *AIAA Journal*, Vol. 46, No. 6, 2008, pp. 1365–1370.
doi:10.2514/1.30154
- [28] Larchevêque, L., Dupont, P., De Martel, E., Garnier, E., and Debièvre, J. F., "Experimental and Numerical Study of Unsteadiness in Boundary Layer/Shock Wave Interaction," *Turbulence and Interactions, Proceedings of the TI 2009 Conference*, edited by M. Deville, T.-H. Lê, and P. Sagaut, Springer, New York, 2010, pp. 263–269.
- [29] Sagaut, P., Garnier, E., Tromeur, E., Larchevêque, L., and Labourasse, E., "Turbulent Inflow Conditions for Large-Eddy Simulation of Supersonic and Subsonic Wall Flows," *AIAA Journal*, Vol. 42, No. 3, 2004, pp. 469–477.
doi:10.2514/1.3461
- [30] Erengil, M. E., and Dolling, D. S., "Unsteady Wave Structure Near Separation in a Mach 5 Compression Ramp Interaction," *AIAA Journal*, Vol. 29, No. 5, May 1991, pp. 728–735.
doi:10.2514/3.10647
- [31] Dussauge, J. P., Dupont, P., and Debièvre, J. F., "Unsteadiness in Shock Wave Boundary Layer Interactions with Separation," *Aerospace Science and Technology*, Vol. 10, 2006, pp. 85–91.
doi:10.1016/j.ast.2005.09.006
- [32] Thomas, F. O., Putnam, C. M., and Chu, H. C., "On the Mechanism of Unsteady Shock Oscillation in Shock Wave/Turbulent Boundary Layer Interaction," *Experiments in Fluids*, Vol. 18, No. 1, 1994, pp. 69–81.
doi:10.1007/BF00209362
- [33] Debièvre, J. F., and Dupont, P., "Dependence Between Shock and Separation Bubble in a Shock Wave/Boundary Layer Interaction," *Shock Waves*, Vol. 19, No. 6, 2009, pp. 499–506.
doi:10.1007/s00193-009-0232-8
- [34] Bailly, C., Lafon, P., and Candel, S., "Subsonic and Supersonic Jet Noise Predictions from Statistical Source Models," *AIAA Journal*, Vol. 35, No. 11, 1997, pp. 1688–1696.
doi:10.2514/2.33